

Long-Term Effects of Nanoscale Magnetite on Human Forebrain-like Tissue Development in Stem-Cell-Derived Cortical Spheroids

Elizabeth D. Henderson,[†] Timothy Hua,[†] Sonia Kiran,[†] Zahraa I. Khamis, Yan Li,^{*} and Qing-Xiang Amy Sang^{*}

Cite This: *ACS Biomater. Sci. Eng.* 2022, 8, 801–813

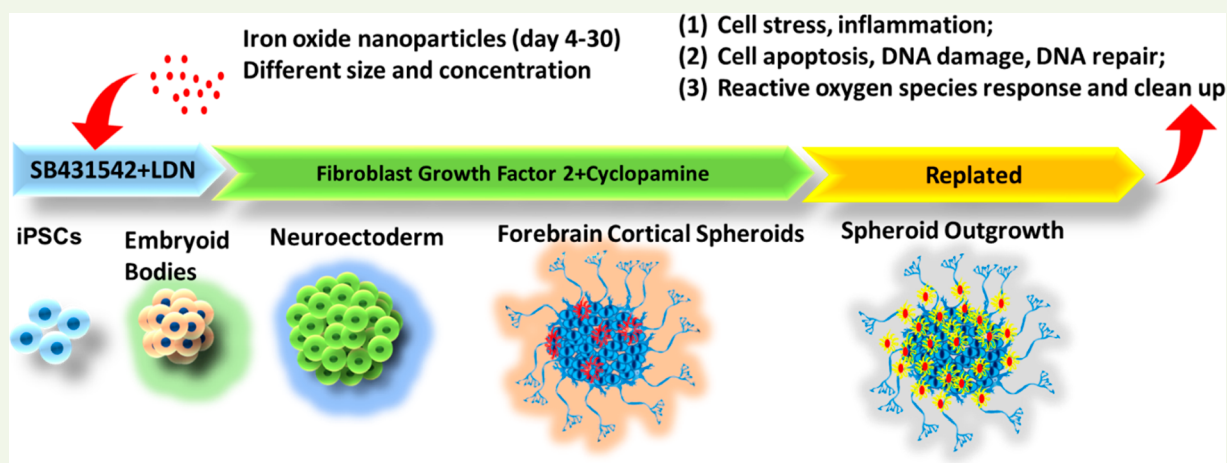
Read Online

ACCESS |

Metrics & More

Article Recommendations

Supporting Information



ABSTRACT: The environmental nanoscale iron magnetite may contribute to the risk of developing neurodegenerative diseases. In addition, iron oxides can be used as the contrast agents in magnetic resonance imaging of neural tissues. The potential long-term impact of nanoscale iron oxides on cellular stress and neuro-inflammation remains unknown. The objective of this study is to evaluate the long-term effects of nanoscale iron oxide exposure on human pluripotent stem cell-derived cortical spheroids that mimic human forebrain-like tissue development. In particular, the cortical spheroids were treated with 8 nm and 15–20 nm magnetite at 0.023, 2.3, and 23 $\mu\text{g}/\text{mL}$ for 4–30 days. The cell viability did not show significant differences among different test groups. The neuronal marker β -tubulin III, cell proliferation marker Ki67, and antioxidant enzyme SOD2 did not show significant changes either. The molecular levels of cellular stress, inflammation, cell apoptosis, DNA damage and repair, and the reactive oxygen species (ROS) response were measured. A negative effect (i.e., increased inflammation and ROS response genes) of 8 nm iron oxide exposure and a positive effect (i.e., decreased inflammation, apoptosis, and ROS response and clean up genes) for 15–20 nm iron oxide exposure were observed. It is postulated that the intracellular iron content and the aggregation of iron oxides contribute to the observed differential response. Although our results demonstrate similar intracellular iron content for 8 nm and 15–20 nm groups, the aggregation is more severe for the 8 nm group (~ 500 nm) than the 15 nm group (~ 220 – 250 nm). Therefore, our data indicate an iron oxide aggregate size-dependent effects on cellular stress, inflammation, cell apoptosis, DNA damage, and the ROS response in the developing human forebrain-like tissue.

KEYWORDS: human pluripotent stem cells, cortical spheroids, magnetite, nanoscale iron oxides, cellular stress, neuro-inflammation

1. INTRODUCTION

Iron is the most abundant transition metal found in the brain and is essential for normal brain development. It participates in myelination, neurotransmitter synthesis, nerve impulse transduction, and energy metabolism.¹ Iron deprivation during pregnancy and infancy can lead to long-term neuro-developmental abnormalities, despite iron supplementation.² Current diagnosis and treatment methods depend solely on the detection of anemia, which is the last stage in iron deficiency. Thus, the developing brain suffers from an iron deficit long before the

onset of anemia because of the prioritization of the red blood cells for iron during negative iron balance.³ However, this

Received: November 23, 2021

Accepted: January 10, 2022

Published: January 24, 2022



essential biometal, if in excess, can contribute to various neurodegenerative diseases ranging from Alzheimer's disease (AD) to Parkinson's disease, Huntington's disease, and Amyotrophic lateral sclerosis (ALS). The neurodegenerative effect of iron overload in the brain is attributed to free radical formation and subsequent oxidative damage to neuronal cells.⁴ So, it is imperative to maintain iron homeostasis in the brain to ensure proper development of cognitive, motor, social, and educational skills in children. In addition, iron oxides have been used as the contrasting agents in the magnetic resonance imaging of human brain tissue for cell therapy of neurological diseases.^{5,6} This practice can introduce iron into brain metabolism and its long-term effects on brain cell stress and degeneration remain unknown.

Neurodegenerative diseases can arise from genetic predisposition, environmental factors, or a combination of both.⁷ Air pollution is demonstrated to adversely affect the cognitive and behavioral development in children and to impose cognitive impairment and a higher risk of dementia in the elderly (reviewed extensively by Bert et al.).⁸ Epidemiological studies support a link between exposure to air pollution and the incidence of neurodegenerative diseases. A large population-based study in Canada found an increase in dementia cases among people residing close to major traffic roads.⁹ Recently, Crous-Bou et al. reported changes in specific regions of the brain prone to AD in response to air pollutants.¹⁰ In Mexican cities, exposure to high doses of airborne fine particulate matter resulted in gait and balance dysfunction in 75% of young urbanites, increasing their susceptibility to developing AD later in life.¹¹

Out of the airborne particulate matter, nanoparticles (NPs) constitute the greatest hazard to human health. Their small dimensions, high surface area, and variable composition render them highly reactive and able to penetrate any organ, tissue, or cell. Iron-bearing nanoparticles are of particular interest in neurobiology, given the pervasive effect of iron on brain health and disease. Iron NPs can cross the blood–brain barrier from blood circulation, be directly injected into the brain for therapeutic purposes, or be inhaled by the nose and taken up into the brain via the olfactory bulb.¹² Initially, it was thought that all iron NPs, specifically iron oxide or magnetite, found in the brain originate endogenously by biological processes. However, a recent study showed that magnetite nanoparticles identified in the frontal cortex of human brains were spherical, unlike their euhedral biogenic counterparts, indicating an external pollution-derived source. These brain magnetites, associated with nonendogenous metals, were externally deposited from combustion reactions of iron-containing material.¹³ Their morphologies precisely matched the magnetite nanospheres available ubiquitously in airborne particulate matter.¹³ Given their nanoscale dimensions, neurotoxicity, and environmental abundance, iron NPs may inflict serious problems on society by affecting children's development and predisposing adolescents and adults to neurodegenerative diseases.

In this study, an *in vitro* 3D model of the human brain^{14,15} was used to gain a better understanding of its development in the presence of iron oxide NPs. Human-induced pluripotent stem cells (hiPSCs) have been used since 2013 as a promising tool to model, at least, part of the features of the human brain in 3D organoid cultures.^{16–18} Our previous study evaluated the short-term (2–3 days) effects of human cortical spheroids exposure to nanoscale iron oxides.¹⁹ Going one step further, this study

evaluated the effects of long-term iron oxide exposure (24–26 days) on human cortical spheroids, which can mimic the effects of iron NPs on the developing brain. Following the neural differentiation of hiPSCs, 8 nm and 15–20 nm magnetite iron oxides (Fe₃O₄) were added to the human forebrain cortical spheroid/organoid cultures established in our previous studies.^{20–22} Cell viability, proliferation, and oxidative enzyme expression were evaluated. In particular, the molecular levels of iron oxide effects on cellular stress, inflammation, cell apoptosis, DNA damage, DNA repair, and the reactive oxygen species (ROS) response in developing human forebrain-like tissue were investigated. To understand the mechanism of our observation, we measured intracellular iron and iron oxide aggregation, showing the dominating effects of iron oxide aggregation. The significance of this study lies in identifying environmental factors that may impact neurodegeneration, neurotoxicity, neural imaging, and brain organoid-based disease modeling and drug screening.

2. MATERIALS AND METHODS

2.1. Culture of hiPSCs. Human iPSK3 cells were derived from human foreskin fibroblasts transfected with plasmid DNA encoding reprogramming factors OCT4, NANOG, SOX2, and LIN28 (kindly provided by Dr. Stephen Duncan, Medical College of Wisconsin).^{23,24} Human iPSK3 cells were maintained in mTeSR Plus serum-free medium (StemCell Technologies, Inc., Vancouver, Canada) on growth factor-reduced Geltrex-coated surface (Life Technologies) with daily media change. The cells were passaged by Accutase every 7 days and seeded at 1×10^6 cells per well of six-well plate in the presence of rho-associated protein kinase (ROCK) inhibitor Y27632 (10 μ M, Sigma) for the first 24 h.^{25–27}

2.2. Preparation of Iron Oxide Nanoparticles. Two different sizes of magnetite (Fe₃O₄) nanoparticles used were 8 nm (US Nanotechnologies, US3208) and 15–20 nm (US Nanotechnologies, US3230). A stock suspension of 2.3 mg/mL per nanoparticle size was prepared by suspending the nanoparticles in ultrapure water. The stock suspensions were then exposed to ultraviolet radiation overnight to sterilize the materials. The stocks were sonicated in a water bath sonicator at 40 °C for 20 min. Three dilutions were prepared by doing a serial dilution of the original stock in DMEM plus 2% B27 and antibiotics. The final concentrations of the magnetite were 0.023, 2.3, and 23 μ g/mL for each nanoparticle size used.¹⁹ According to our previous studies,^{28,29} the intracellular labeling efficiency for microsized particles of iron oxides (MPIO) can reach 50–80%. It was estimated that the intracellular labeling efficiency for nanoscale iron oxides should be similar or higher than that for MPIO.

Dynamic light scattering (DLS) of iron oxide magnetite was performed to measure the actual diameter and polydispersity of magnetite particles in the suspension. The 15 and 8 nm size magnetite were suspended in deionized water and sonicated for 10 min at room temperature. The suspension was further diluted and transferred to the cuvette for DLS using a Brookhaven dynamic light scattering apparatus (Brookhaven Instruments Corp, Holtsville, NY), and the results were obtained from *Particle Explorer* software.

2.3. Differentiation of hiPSCs into Cortical Spheroids. Human iPSK3 cells were seeded into ultralow attachment (ULA) 24-well plates at 3×10^5 cells/well in Dulbecco's modified Eagle medium/nutrient mixture F-12 (DMEM/F-12) plus 2% B27 without antioxidant serum-free supplement (Life Technologies). For the first 24 h, rho-associated protein kinase (ROCK) inhibitor Y27632 (10 μ M, Sigma) was added to promote cell survival and the formation of embryoid bodies (EB). On day 1, the EBs were treated with dual SMAD signaling inhibitors SB431542 (10 μ M, Sigma) and LDN193189 (10 μ M, Sigma). The media were changed every other day thereafter. From day 8 until day 30, the spheroids were treated with fibroblast growth factor (FGF) 2 (10 ng/mL, Life Technologies) and Sonic hedgehog inhibitor cyclopamine (1 μ M, Sigma) for the cortical forebrain differentiation.^{20,21,30} In

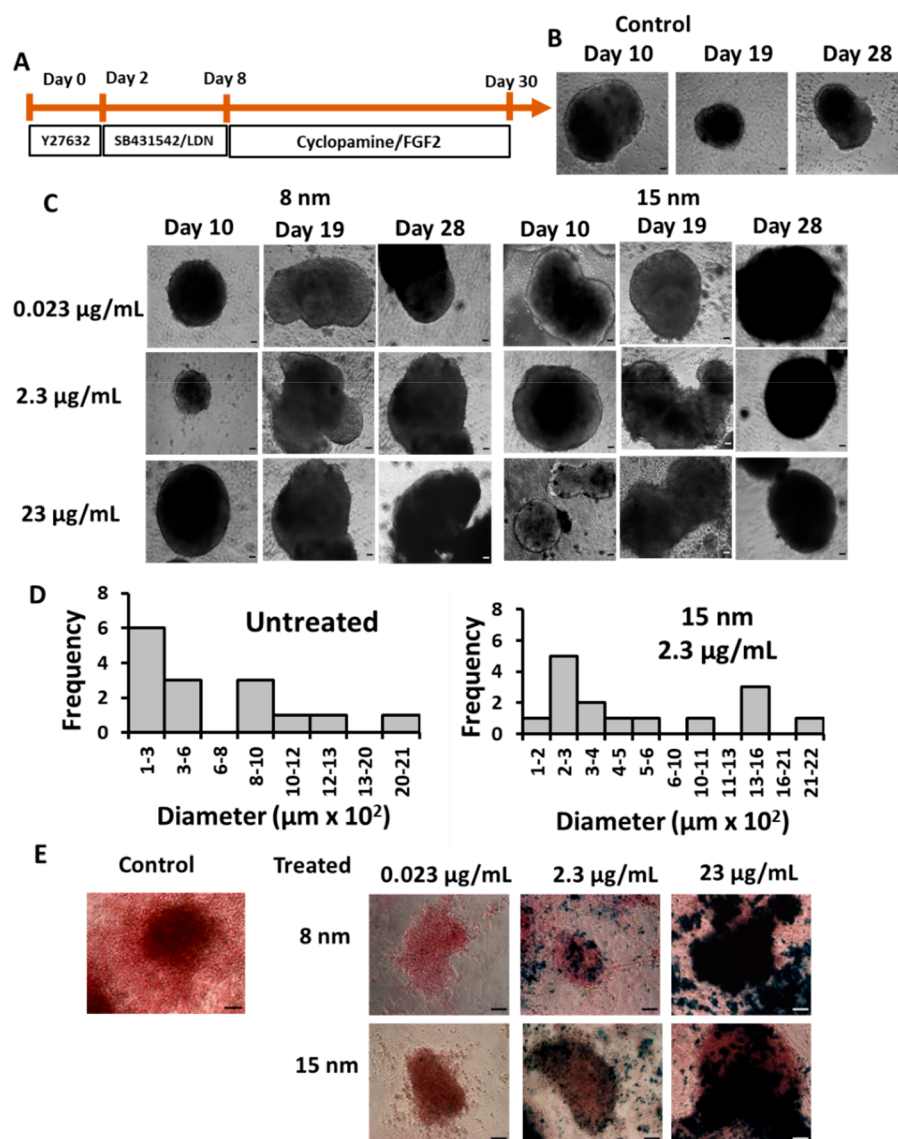


Figure 1. Cortical differentiation from human iPSCs. (A) Schematic illustration of the cortical spheroid differentiation. LDN: LDN193189. (B) Phase-contrast images of the untreated and (C) the nanoparticle-treated cortical spheroids. The nanoparticles were added from day 4 until day 30 of culture. (D) Representative spheroid size distribution during the differentiation (day 26) in the presence of nanoparticles. (E) Iron staining images of the untreated and the nanoparticle-treated cortical spheroids (day 30) replated on a Matrigel-coated surface. Scale bar: 100 μm .

addition, for the tested conditions, the spent media were replaced by the fresh media containing iron oxides nanoparticles (at different size and concentrations) every two or three days during cortical spheroid differentiation from day 4 to day 30. The spheroids were used for various characterizations.

The images of cortical spheroids (exposed to iron oxides or the untreated control) were captured during the differentiation by a phase contrast microscopy. The captured images were converted to binary images using *ImageJ* software (<http://rsb.info.nih.gov/ij>) and analyzed with the “particle analysis tool”. Through particle analysis in *ImageJ* software, the Feret’s diameter of each aggregate in the images was calculated, which provides the size distribution of the aggregates.

2.4. Live/Dead Staining. The cells were evaluated for viability using a Live/Dead staining kit (Molecular Probes) according to the manufacturer’s protocol. After treating with nanoparticles, the replated spheroids were washed with phosphate-buffered saline (PBS) and then incubated in DMEM-F12 containing 2 μM calcein-AM (green) and 0.8 μM ethidium homodimer I (red) for 20–25 min at room temperature and protected from light. The images were taken under a fluorescent microscope (Olympus IX70, Melville, NY). For flow cytometry

quantification, the spheroids were trypsinized and about 1 million cells were aliquoted in one sample for incubation with calcein-AM (green) and ethidium homodimer I (red),

2.5. Iron Staining Assay. The cells were evaluated for the detection of iron oxide using an iron staining kit (Abcam). After 48 h, the cells were incubated with the working solution for 3 min at room temperature. After the cells were washed with PBS, the nuclear fast red solution was added to the cells and incubated for 5 min at room temperature. The cells were rinsed with PBS four times before images were taken.

2.6. 3-(4,5-Dimethylthiazol-2-yl)-2,5-diphenyltetrazolium Bromide (MTT) Assay. After treatment with nanoparticles, the replated neural cells were incubated with a 0.5 mg/mL MTT (Sigma) solution for an hour at 37 $^{\circ}\text{C}$. The media and MTT were removed. The formazan crystals were dissolved in dimethyl sulfoxide and centrifuged at 800 g for 5 min. The absorbance of the supernatants was measured at 490 nm on a microplate reader (BioRad Laboratories, Hercules, CA).

2.7. Immunocytochemistry. For biomarker detection, the cells were fixed using 5% paraformaldehyde (PFA) and permeabilized using 0.2% Triton-X 100. The samples were blocked with 5% FBS in PBS

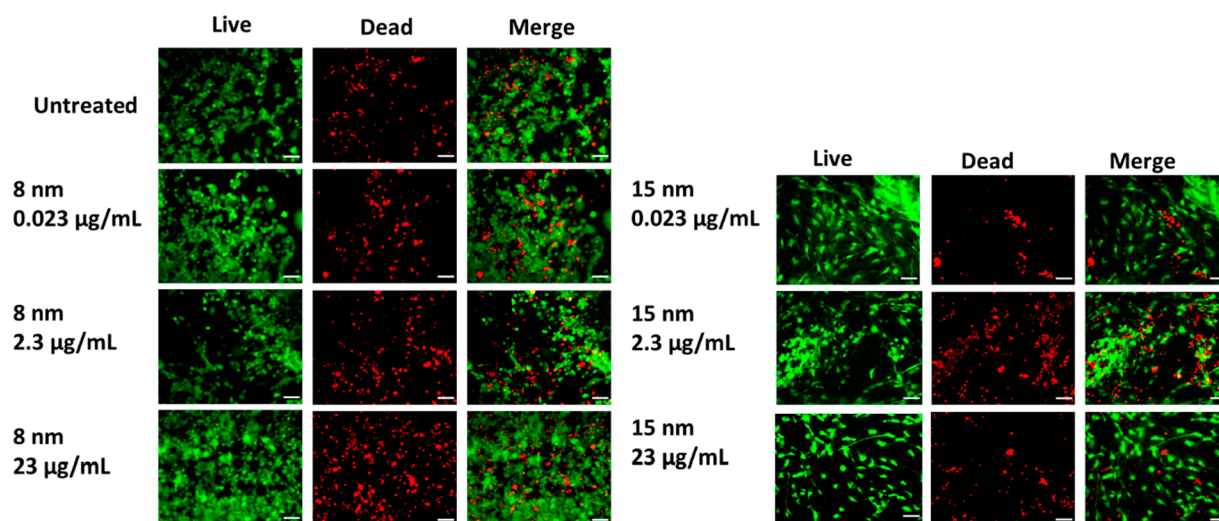


Figure 2. Live/Dead images of the control and the nanoparticle-treated cortical spheroids. The day 30 cortical spheroids were plated on a Matrigel-coated surface for 2 days in the presence of the nanoparticles. Ethidium homodimer-1 and calcein-AM were used to stain dead and live cells, respectively, for the control, 8 nm, and 15 nm nanoparticle-treated cortical spheroids. Scale bar: 25 μm .

and stained with the primary antibodies (Table S1), followed by the corresponding antispecies Alexa Fluoro antibodies, i.e., Alexa Fluor 488 goat antimouse IgG1 or Alexa Fluor 594 goat anti-Rabbit IgG (Life technologies). Both primary and secondary antibody dilutions were made based on the manufacturer's recommendations and prepared in staining buffer (2% FBS in PBS). The nuclei were then counterstained with Hoechst 33342 (blue), and pictures were taken for blue, green, and red colors to detect the markers and their cellular locations under a fluorescent microscope (Olympus IX70, Melville, NY).

2.8. Flow Cytometry. Two-color flow cytometry was used to analyze green fluorescence for calcein-AM (ex/em \sim 495 nm/ \sim 515 nm) and the red fluorescence for ethidium homodimer-1 (ex/em \sim 495 nm/ \sim 635 nm) for cells stained using Live/Dead assay. The cells were acquired with the BD FACSCanto II flow cytometer (Becton Dickinson, Franklin Lakes, NJ) and analyzed using *FlowJo* software. For immunophenotyping, flow cytometry analysis of β -tubulin III, Ki67, and SOD2 was performed. Briefly, trypsinized cells were fixed with 5% PFA for about 15 min and permeabilized with 100% cold methanol for 15–30 min. The samples were blocked with 5% FBS in PBS and then stained with the corresponding marker antibody overnight. After washing, the samples were incubated with the secondary Alexa Fluor 488 or 594 antibody for 1 h. After washing, the samples were taken for flow cytometry measurement. The cells were acquired with a BD FACSCanto II flow cytometer and analyzed against isotype control using *FlowJo* software.

2.9. Measurement of Reactive Oxygen Species (ROS). An Image-iT LIVE green reactive oxygen species detection kit (Molecular Probes I36007) was used to detect reactive oxygen species after exposure of spheroids to the magnetite nanoparticles. Briefly, a 25 μM carboxy-H₂DCFDA working solution was prepared from a 10 mM solution and used to label single-cell suspensions after spheroid trypsinization. The cells were incubated in the dark for 30 min and then measured immediately using flow cytometry. Alternatively, the cells were counterstained with Hoechst 33342 and imaged under a fluorescent microscope.

2.10. Reverse Transcription-Polymerase Chain Reaction (RT-PCR) analysis. Total RNA was isolated from the neural cell samples exposed to iron oxides using the RNeasy mini kit (Qiagen, Valencia, CA) according to the manufacturer's protocol, followed by treatment with the DNA-Free RNA kit (Zymo, Irvine, CA). Reverse transcription was carried out using 2 μg of total RNA, anchored oligo-dT primers, and Superscript III (Invitrogen, Carlsbad, CA) according to the manufacturer's protocol. Primers were specific to the targeted genes: *COMT*, *BDNF*, *MAPK11/14*, *ATM*, *Nfkb1/2*, *TPS3*, *XPC*, *CAT*, *CAPS3/6*, and *SOD1*. The primers were designed using the software

Primer-BLAST (NIH Database) (Table S2). The gene β -actin was used as an endogenous control for normalization of expression levels. RT-PCR reactions were performed on an ABI7500 instrument (Applied Biosystems, Foster City, CA), using SYBRI green PCR master mix (Applied Biosystems). The amplification reactions were performed as follows: 2 min at 50 $^{\circ}\text{C}$; 10 min at 95 $^{\circ}\text{C}$; and 40 cycles of 95 $^{\circ}\text{C}$ for 15 s; 55 $^{\circ}\text{C}$ for 30 s; and 68 $^{\circ}\text{C}$ for 30 s. The Ct values of the target genes were first normalized to the Ct values of the endogenous control β -actin. The corrected Ct values were then compared for the treatment conditions to the untreated control. Fold changes in gene expression was calculated using the comparative Ct method: $2^{-(\Delta\text{Ct}_{\text{treatment}} - \Delta\text{Ct}_{\text{control}})}$ to obtain the relative expression levels.

2.11. Inductively Coupled Plasma Mass Spectrometry (ICP-MS). To measure the intracellular iron content, we performed ICP-MS. The standard solutions with concentration 0, 0.5, 1, 2.5, 5, and 10 ppb were first prepared by dissolving Fe(III) chloride in 2% w/v nitric acid (trace metal grade from Fisher Sci, Cat#A509–500) prepared with ultrapure water (HPLC grade). The samples were prepared by washing spheroids five times with PBS and once with 0.66 g/L oxalic acid at 50 $^{\circ}\text{C}$ for 10 min to remove magnetite present outside spheroids. The cells were then lysed in radioimmunoprecipitation assay buffer (RIPA) and centrifuged at 15 000 rpm for 10 min to make sure everything settled. The supernatant was removed and the samples were dissolved in 0.66 g/L oxalic acid at 50 $^{\circ}\text{C}$ for 30 min to dissolve intracellular iron content. Two percent nitric acid was then added to the samples to make a total volume of 5 mL. The samples were then analyzed using an iCAP RQ ICP-MS instrument and software.

2.12. Statistical Analysis. The representative experiments are presented, and the results are expressed as [mean \pm standard deviation]. To assess the statistical significance, we performed one-way ANOVA followed by Fisher's LSD post hoc tests. A p -value < 0.05 was considered statistically significant.

3. RESULTS

3.1. Cortical Spheroid Differentiation and Magnetite Uptake. At the initial stage of differentiation, a ROCK inhibitor was added to the iPSK3 cells to increase cell survival and the EB formation. Sequentially, dual SMAD inhibitor treatment of SB431542 and LDN193189 was used to promote neural ectodermal commitment. Then, sonic hedgehog antagonists cyclopamine and FGF2 were used to promote neural progenitor and cortical differentiation of the spheroids (Figure 1A, B). Two sizes of magnetite (8 and 15 nm) at three different

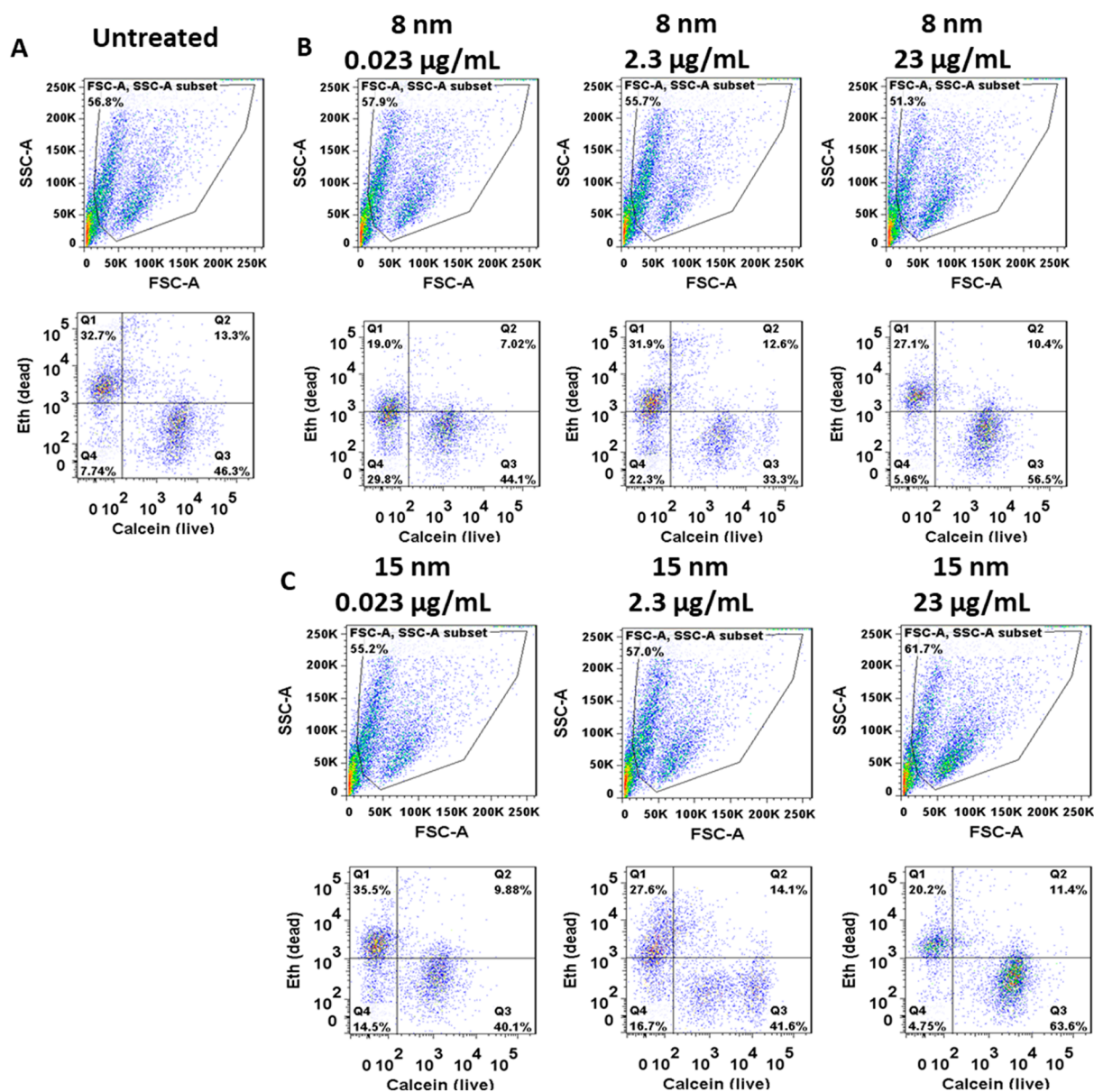


Figure 3. Two-color flow-cytometry analysis for Live/Dead assay of the 8 and 15 nm magnetite treated cortical spheroids (day 30). (A) Untreated, (B) treated with 8 nm magnetite, and (C) treated with 15 nm magnetite.

concentrations (0.023, 2.3, and 23 $\mu\text{g/mL}$) were added to the culture from day 4 until day 30 (Figure 1C). The cortical spheroid size ranged from 500 μm to 1.2 mm, and its development did not seem to be affected by the incorporation of the nanoparticles (Figure 1D and Figure S1). However, more single cells were released from the spheroids as the particle concentration increased along with the differentiation.

To observe iron oxide-cell interaction, the day 30 cortical spheroids were replated on Matrigel, and iron staining was performed to detect iron oxides that might have been taken inside the cells. The nucleus showed a red color due to nuclear fast red solution, whereas the iron oxides were represented as dark blue because of Prussian blue. As expected, the higher the concentration of magnetite, the more iron oxides were taken up by the cells regardless of the particle size (Figure 1E).

3.2. Effect of Magnetite on Cell Viability. The cell viability was evaluated using the Live/Dead assay. Live cells

stained with calcein AM appeared in green fluorescence, whereas dead cells were stained with ethidium homodimer-1 and colored in red. The presence of dead cells was observed in all groups without consistent differences (Figure 2). The cell viability of the treated cortical spheroids was further quantified using two-color flow cytometry after dissociation (Figure 3). The proper color compensation was shown in Figure S2. The percentage of dead cells was shown in Q1 gate and ranged from 19.0 to 35.5% for all the nanoparticle treated groups, in comparison to 32.2% of the control group (untreated). For 8 nm treatments, flow cytometry results from another two experiments (Figure S2) also showed similar viability at different concentrations, which was not lower than untreated control despite experiment to experiment variations. MTT assay for cell metabolic activity did not show consistent concentration-dependent trends either (Figure S3). Within the 8 nm groups, the 23 $\mu\text{g/mL}$ treatment showed a significantly higher level of

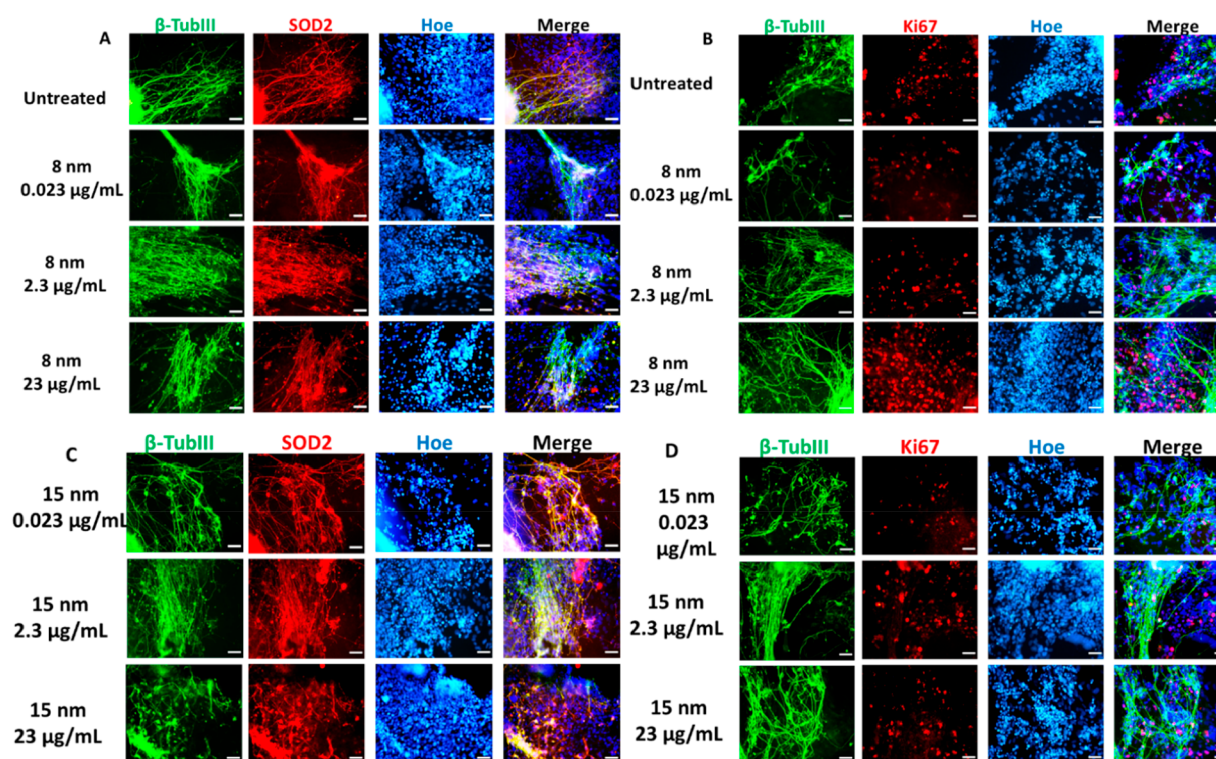


Figure 4. Immuno-fluorescent images of β -tubulin III, SOD2, and Ki67 for replated day 30 cortical spheroids treated with 8 or 15 nm magnetite. The images were taken from outgrowth of day 30 spheroids replated on Matrigel-coated wells for a week, showing axons growing out of the spheroids. Co-localization of (A) β -tubulin III (β -TubIII) and SOD2; (B) β -tubulin III and Ki67 for 8 nm groups. Co-localization of (C) β -tubulin III (β -TubIII) and SOD2; (D) β -tubulin III and Ki67 for 15 nm groups. Scale bar: 50 μm . Hoe: Hoechst 333342 for counterstaining with cell nuclei.

the normalized MTT activity than the 0.023 and 2.3 $\mu\text{g/mL}$ groups. On the other hand, the 23 $\mu\text{g/mL}$ treatment of the 15 nm group showed a significantly lower level of the normalized MTT activity than the 0.023 and 2.3 $\mu\text{g/mL}$ treatment groups. It was thought that the spheroid culture variations may confound the observation of MTT assay. Taken altogether, treatment of cortical spheroids with 8 or 15 nm magnetite at different concentrations did not induce significant cell death compared to the untreated control.

3.3. Effects of Magnetite on Neuronal Cell Proliferation and Antioxidant Enzyme Expression. To further evaluate the biological effects of nanoscale magnetite, we evaluated the colocalization of the neuronal marker β -tubulin III with the cell proliferation marker Ki67 and the antioxidant enzyme SOD2 using immunocytochemistry (Figure 4). On day 30, cortical spheroids treated with 8 nm particles showed a high amount of β -tubulin III- and SOD2-positive cells with axonal morphology (Figure 4A, B), whereas Ki67 expression was low in cells at day 30 due to the prevalence of differentiation. The 15 nm particle treated cortical spheroids showed a similar expression of SOD2 and β -tubulin III, with little Ki67⁺ cells at day 30 (Figure 4C, D).

The quantification of β -tubulin III, SOD2, and Ki67 was performed by flow cytometry (Figure 5). On day 30, cells of cortical spheroids treated with 8 nm nanoparticles had 55.6–65.9% β -tubulin III⁺ cells comparable to the untreated group (64.8%) (Figure 5A). For 15 nm nanoparticle treatment, the middle concentration group had 69.1%, whereas the low and high concentration groups had lower expression (45.4 and 42.5%, respectively). Although exposure to 8 nm nanoparticles did not affect SOD2 expression (94.0–94.2%) compared to

untreated control (92.5%), cells treated with 15 nm nanoparticles had SOD2 expressed in a similar trend to β -tubulin III with the middle concentration group at 91.7%. The low and high concentration groups showed lower expression of 85.3 and 83.0%, respectively (Figure 5B). Consistent with immunocytochemistry, flow cytometry revealed only 3–14% of Ki67⁺ cells on day 30 (Figure S4).

The levels of ROS in the cells for different conditions were quantified by flow cytometry (Figure 6A) and the localization was shown in the images (Figure 6B). The 8 and 15 nm 0.023 $\mu\text{g/mL}$ groups showed comparable expression to the untreated control. For the 8 nm groups, higher concentrations of 2.3 and 23 $\mu\text{g/mL}$ showed about 11–14% decrease in ROS expression. For the 15 nm groups, higher concentrations of 2.3 and 23 $\mu\text{g/mL}$ showed about a 9–10% increase in ROS expression. These results indicate that high concentrations of iron oxides may alter the ROS balance or redox levels.³¹

3.4. Expression of Genes Involved in Different Signaling Pathways in Cortical Spheroids. RT-PCR was used to determine the expression of genes (mRNA levels) that are involved in different cellular pathways, including cellular stress (*BDNF*, *COMT*), inflammation (*NFKB1*, *NFKB2*), cell apoptosis (*CASP3*, *CASP6*), DNA damage (*TP53*), DNA repair (*XPC*), ROS response (*MAPK11*, *MAPK14*, *ATM*), and ROS clean up (*SOD1*, *CAT*). The expression of the ROS response genes, *MAPK11*, *MAPK14*, and *ATM*, increased in a concentration-dependent manner (~1.5 fold) (Figure 7A). This increase in ROS levels and the consequent increase in oxidative stress might be responsible for the higher cellular stress and inflammation observed in treated cells. As for the ROS cleanup genes, *SOD1* showed little increase with particle

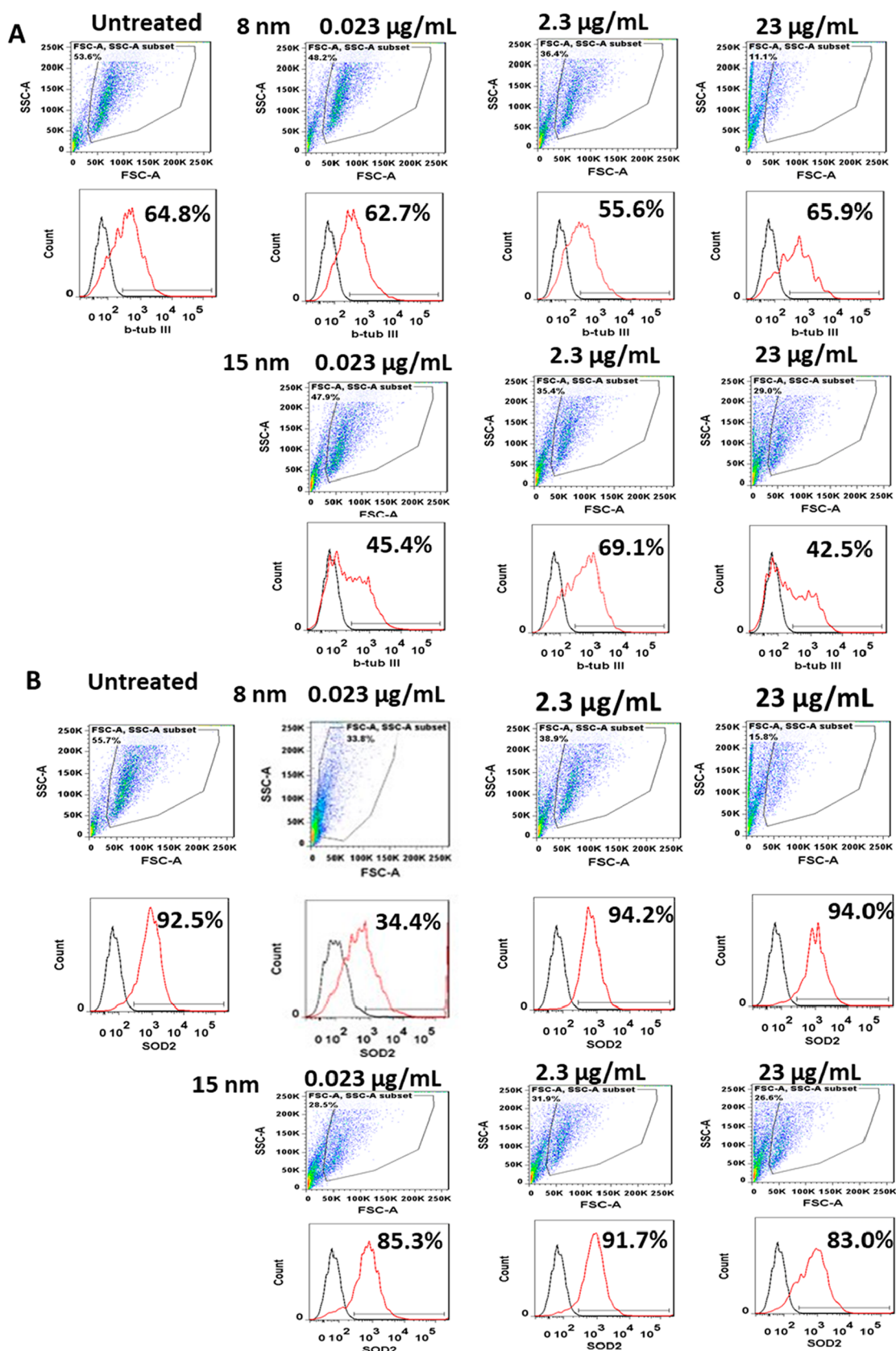


Figure 5. Flow cytometry of beta-tubulin III and SOD2 expression for day 30 cortical spheroids. The spheroids were exposed to 8 and 15 nm iron oxides at different concentrations. (A) Beta-tubulin III (b-tub III); (B) SOD2. Blackline: isotype control.

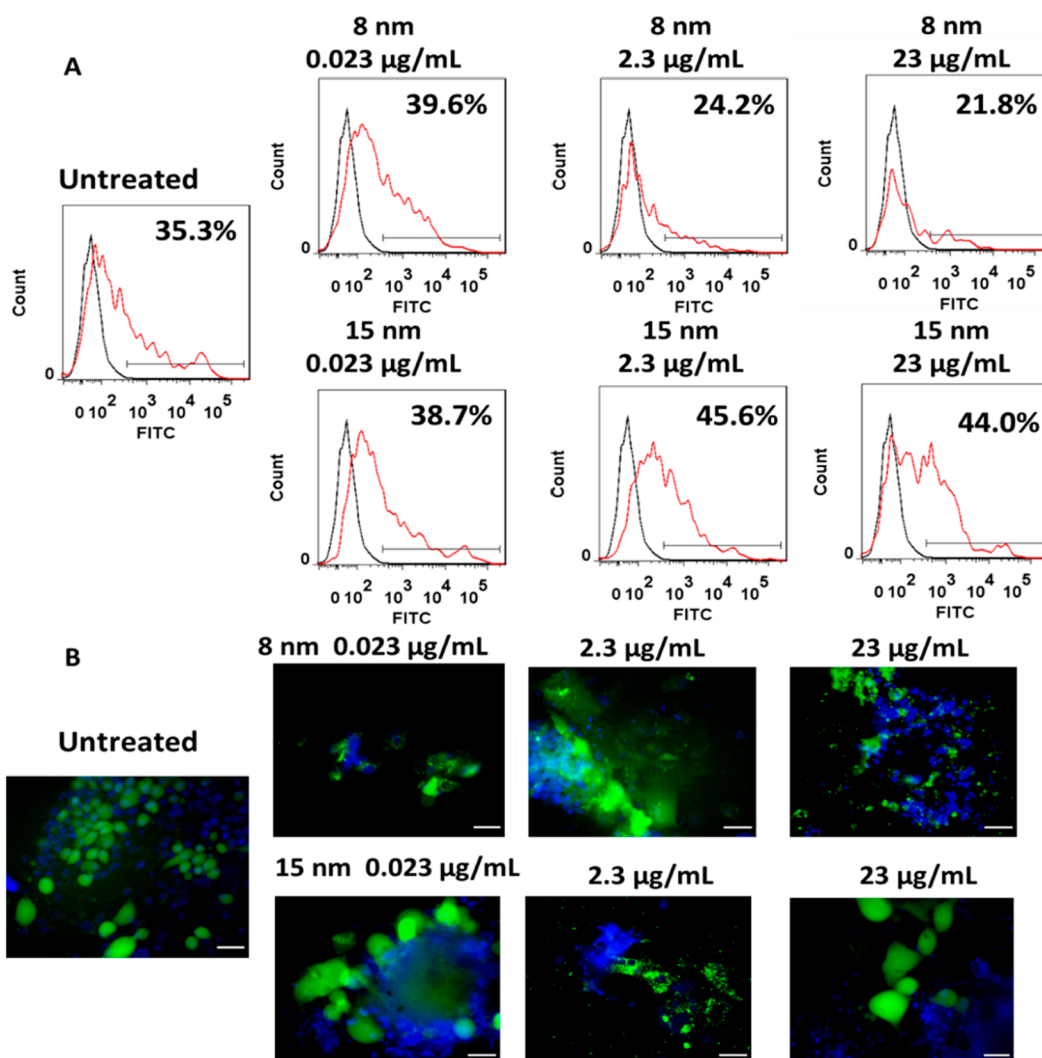


Figure 6. ROS expression for day 30 cortical spheroids in the presence of iron oxides. (A) Flow cytometry analysis of ROS expression for day 30 cortical spheroids. The spheroids were exposed to 8 and 15 nm iron oxides at different concentrations. Blackline: negative control. (B) Fluorescent images of ROS expression. Green, ROS; blue, cell nuclei. Scale bar, 50 μm .

concentration, whereas *CAT* expression exhibited large variations. Only the 2.3 $\mu\text{g/mL}$ group showed a significant 3-fold increase. In comparison to the untreated control, 8 nm exposed cells showed concentration-dependent increase in *COMT*, *BDNF*, *NFKB1*, and *NFKB1* expression (~ 1.5 fold) (Figure 7B). The cell apoptosis-related genes *CASP3* and *CASP6* remained at similar levels for the treated group compared to the untreated control (Figure 7C). However, the DNA damage gene, *TP53*, showed a minor increase for the 2.3 $\mu\text{g/mL}$ group (1.2 fold) but not the 23 $\mu\text{g/mL}$ group. The DNA repair gene *XPC* expression showed a concentration-dependent increase (1.2–1.4 fold).

Comparing the ROS response genes in 15 nm treated cells to the untreated control, *ATM* and *MAPK14* were expressed at similar levels under all conditions (Figure 8A), whereas *MAPK11* showed a significant decrease up to 0.4 fold (i.e., 60%). For ROS clean up, *CAT* showed the most significant decrease up to 0.2 fold (i.e., 80%), whereas *SOD1* expression was comparable to that of the untreated control. Cellular stress genes *COMT* and *BDNF* and inflammation gene *NFKB2* were expressed at comparable levels to the untreated group (Figure 8B), whereas the *NFKB1* (another inflammation gene)

expression was decreased by 30% (~ 0.7 fold) for the 2.3 and 23 $\mu\text{g/mL}$ groups. *CASP3* and *CASP6* (apoptosis-related genes) also showed a decrease of 40% (~ 0.6 fold) for 2.3 $\mu\text{g/mL}$ and 23 $\mu\text{g/mL}$ groups (Figure 8C). *TP53* (DNA damage) exhibited similar expression compared to the control, except for the 2.3 $\mu\text{g/mL}$ group (~ 0.4 fold). *XPC* (DNA repair) expression did not change regardless of the conditions. Taken together, different sizes of magnetite could induce different gene expression profiles in the long-term-treated cortical spheroids.

3.5. Intracellular Iron Content. It was postulated that the iron content per cell might be different for the cells exposed to 8 nm (more excessive) than to 15–20 nm (less excessive) iron oxide particles. Therefore, ICP-MS was performed for the various conditions (Figure 9 and Figure S5). The intracellular iron content increased nonlinearly with the exposure concentration from 0.18 ± 0.03 ng (per cell) to 0.73 ± 0.03 and 2.67 ± 0.01 ng for 0.023, 2.3, and 23 $\mu\text{g/mL}$ of 8 nm groups, respectively. Similarly, it increased from 0.11 ± 0.02 to 0.67 ± 0.02 and 2.54 ± 0.10 ng for 15 nm groups corresponding to different concentrations. These results showed size and concentration-dependent internalization of iron oxide nanoparticles.

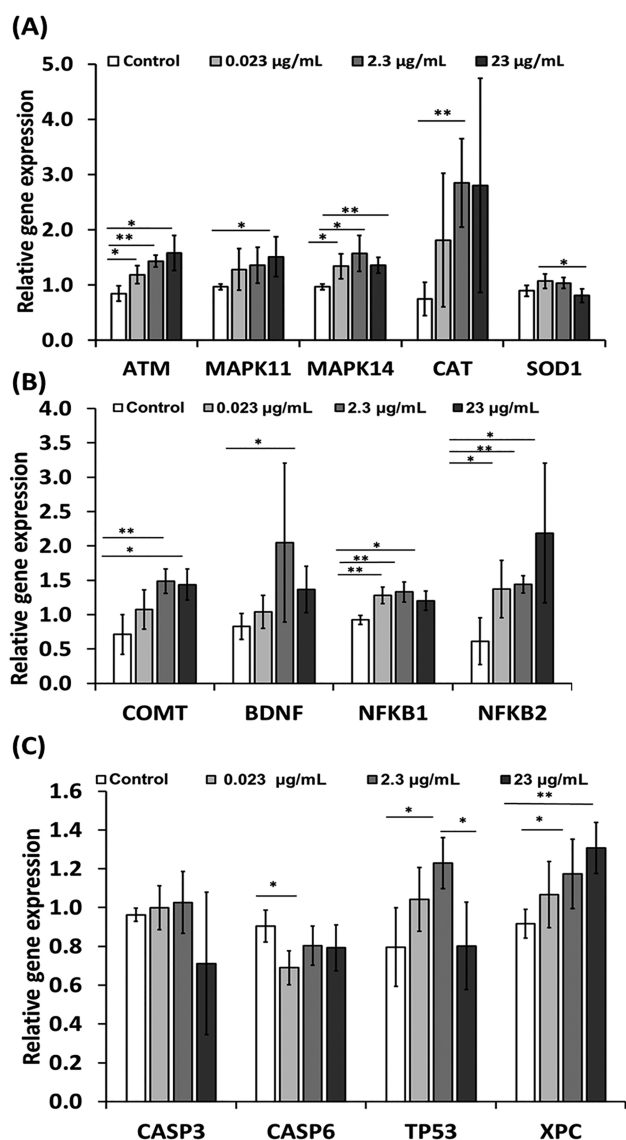


Figure 7. Expression of different genes involved in cellular pathways of the day 30 cortical spheroids exposed to the 8 nm magnetite. The mRNA levels were determined by RT-PCR. The expression of genes that are involved in (A) the ROS response (*MAPK11*, *MAPK14*, *ATM*) and the ROS clean up (*SOD1*, *CAT*); (B) cellular stress (*BDNF*, *COMT*) and inflammation (*NFKB1*, *NFKB2*); (C) cell apoptosis (*CASP3*, *CASP6*), DNA damage (*TP53*), and DNA repair (*XPC*). * and ** indicate the statistical difference with $p < 0.05$ and $p < 0.01$, respectively.

It was postulated that the aggregation of iron oxides might confound their cellular effects. Therefore, DLS of 8 and 15 nm iron oxides was performed (Figure S6). The results confirm the presence of the aggregation of iron oxide nanoparticles. The aggregation is more severe for 8 nm group (~500 nm) than the 15 nm group (~220–250 nm). Therefore, the size of iron oxide aggregates may be attributed to the observed differential cellular response for the 8 and 15 nm groups.

4. DISCUSSION

The objective of this study is to evaluate the long-term effects of nanoscale iron oxide particles of different sizes and concentrations on human forebrain organoids that mimic human brain-

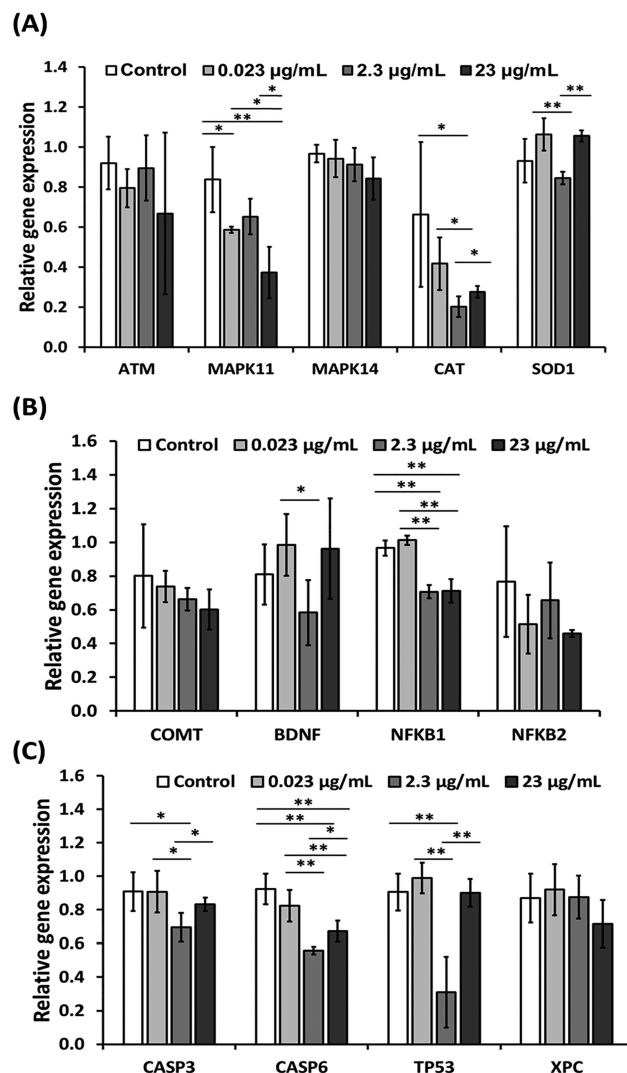


Figure 8. Expression of different genes that are involved in cellular pathways of the day 30 cortical spheroids exposed to the 15–20 nm magnetite. The mRNA levels were determined by RT-PCR. The expression of genes that are involved in (A) ROS response (*MAPK11*, *MAPK14*, *ATM*), and ROS clean up (*SOD1*, *CAT*); (B) cellular stress (*BDNF*, *COMT*), inflammation (*NFKB1*, *NFKB2*); (C) cell apoptosis (*CASP3*, *CASP6*), DNA damage (*TP53*), and DNA repair (*XPC*). * and ** indicate the statistical difference with $p < 0.05$ and $p < 0.01$, respectively.

like tissue development. The viability of the neural cells did not show significant differences among different test groups. However, the results indicate a negative effect on neural cells (i.e., increased inflammation and ROS response genes) from exposure to 8 nm iron oxides but a positive effect (i.e., decreased inflammation, apoptosis, ROS response, and clean up genes) from exposure to 15–20 nm iron oxides. It was postulated that the intracellular iron content per cell and the aggregation of the iron oxides may alter iron metabolism equilibrium in the cells and the associated cellular responses. Our results of intracellular iron content characterization showed a dose-dependent increase in intracellular iron, although the difference between the 8 nm and 15–20 nm groups was small. However, the aggregation is more severe for the 8 nm group (~500 nm) than for the 15 nm group (~220–250 nm), although the exact molecular mechanism for this aggregation process remains to be revealed.

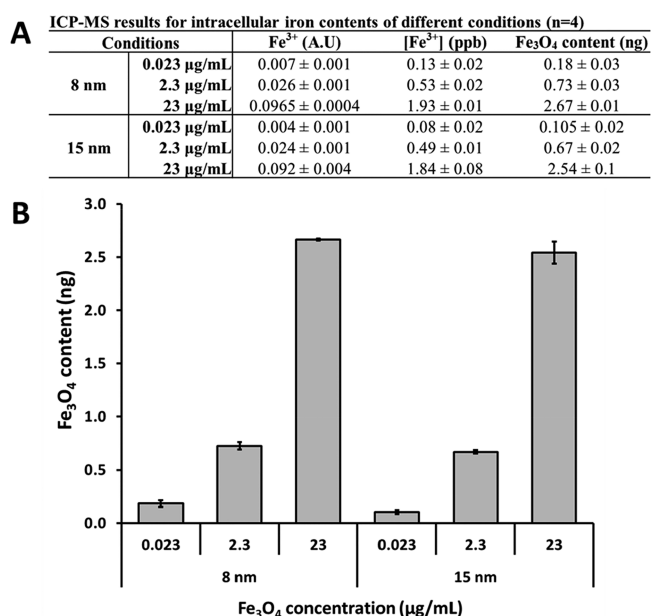


Figure 9. Intracellular iron contents for exposure to different size and concentration of iron oxides. (A) ICP-MS results and (B) graphical representation of intracellular iron contents.

Therefore, the size of aggregated nanoparticles may be attributed to the observed differential cellular response rather than intrinsic nanoparticle size.

Nanoscale iron oxides have been reported to have negative effects, inducing oxidative stress, DNA damage, and caspase activation.^{5,32} A study has shown that nanoparticles less than 35 nm can penetrate the blood–brain barrier.³³ Although transition metals (iron) are essential in many biological reactions, alterations in their homeostasis result in increased free radical production.³⁴ Iron and copper transfer single electrons as they cycle between their reduced (Fe²⁺, Cu¹⁺) and oxidized (Fe³⁺, Cu²⁺) states, and this redox cycling can catalyze the production of reactive oxygen species.³⁵ Iron accumulation could be an important contributor to the oxidative damage of Alzheimer's disease (AD),³⁶ leaning to neurodegeneration.³⁷ The high metal content of the central nervous system makes it particularly susceptible to metal-catalyzed oxidative damage, protein aggregation, neurotoxicity, and neurodegeneration. Metals promote both precipitation and deposition of amyloid-beta (A β) and oxidative stress, which is associated with the neuritic plaques.^{38–44} Oxidative stress has been identified to increase levels of lipid peroxidation,⁴⁵ protein carbonyl,⁴⁶ and DNA damage.⁴⁷ A few studies, performed on human and mice exposed to air-containing particulate matter, showed a potential correlation of this exposure to AD.^{48,49} The mechanism of direct interaction of magnetite with DNA has not been investigated yet, but the size- and concentration-dependent toxicity has been observed to cause genetic mutations and DNA damage.⁵⁰ Our study observed mild cellular stress and inflammation on neural cells after 26-day exposure to 8 nm iron oxide particles, which is a very short period compared to the duration (years) of exposure to environmental iron magnetite in an individual's life.

Nanoscale iron oxides have also been reported to have positive effects on the cells that uptake them.^{6,51} The internalization of iron oxides (12 nm or 20–30 nm) by mesenchymal stem cells stimulated various growth factors, including angiopoietin-1 (ANG-1), FGF2, hepatocyte growth

factor, vascular endothelial growth factor, platelet-derived growth factor, transforming growth factor, neurotrophin-3, and brain-derived neurotrophic factor (BDNF), or abrineurin, exerting the antiapoptotic, anti-inflammation, and neurotrophic effects for stroke therapy and cardiac repair.^{6,51} Iron is also required as a cofactor in the central nervous system metabolic processes, including oxidative phosphorylation, neurotransmitter production, nitric oxide metabolism, and oxygen transport.⁵² It was suggested that the stimulated phosphorylation of JNK and c-Jun signaling molecules may contribute to the positive effects of the iron oxides.^{6,51} The results from the current study indicate mild effects on neuro-inflammation, apoptosis, and redox regulation at a molecular level in the cells treated with 15 nm particles. Therefore, the right size of iron oxides needs to be carefully designed to exploit their beneficial effects as the contrast agent in magnetic resonance imaging for in vivo cell tracking.

Day 30 cortical spheroid exposure to 8 nm iron oxides did not seem to have effects on β -tubulin III and SOD2 expression, whereas exposure to 15 nm iron oxides resulted in similar or lower expression of β -tubulin III and SOD2. As the lower expression was not concentration-dependent, it was thought that the culture variations might contribute to the observed expression levels. The current suspension culture system of cortical spheroids was used because it is simple, scalable, and easy to operate. State-of-the-art organ-on-a-chip systems featuring combination of perfusable vasculature and brain organoids may be used in the future.

Our results show that the CAT gene increases in a concentration-dependent manner, whereas the SOD1 gene does not change with iron oxide concentration. SOD deals with ROS first by converting superoxide to H₂O₂, which breaks into water by CAT. At the time cells were analyzed, SOD might already have produced H₂O₂, triggering higher expression of CAT gene.^{53,54} The presence of oxidative species and the resultant oxidative stress has been observed through flow cytometry analysis of ROS generation. Although the ROS response and clean up genes decreased with exposure to 15 nm iron oxides, a slight increase in ROS levels quantified by flow cytometry was observed. Instead of simply increasing the oxidative stress, the presence of iron oxides was thought to alter the ROS balance or redox level compared to that of the untreated culture. The slight increase in the ROS expression may be beneficial to neural differentiation.³¹

For some gene expression such as CAT in Figure 7, large variations were observed, which could be attributed to the variability of cortical spheroids. Brain organoids derived from human pluripotent stem cells are useful for disease modeling in order to evaluate neurodegenerative diseases.⁵⁵ However, one of the challenges with organoid engineering is the organoid reproducibility^{56,57} and cell diversity within the organoids.^{58,59} Our study used the low attachment 24-well plates and the initial size of cortical spheroids was not controlled. Controlling the initial cell number for cortical spheroid formation,⁵⁹ single spheroid formation in 96-well plate or microfluidic system⁶⁰ may improve the reproducibility of 3D spheroid models. Moreover, the cortical spheroid model used in this study lack the microglia component and the blood–brain barrier. The neural cell–iron oxide interactions and the immune response could be better represented in the presence of microglia and other cell types.²²

5. CONCLUSION

This study evaluated the potential role of nanoscale iron magnetite on the tissue development of human forebrain spheroids/organoids. A negative effect (i.e., increased inflammation and ROS response genes) from exposure to 8 nm iron oxides and a positive effect (i.e., decreased inflammation, apoptosis, and ROS response) from exposure to 15–20 nm iron oxides were observed. These results indicate iron oxide aggregate size-dependent effects of iron oxides on cellular stress, inflammation, cell apoptosis, DNA damage, DNA repair, and the reactive oxygen species response in the developing human forebrain-like tissue. As a potential environmental factor for neurodegeneration, depletion of small iron magnetite in the environment might be important. As a contrasting agent in magnetic resonance imaging, the properties of iron oxides need to be carefully designed and administered to promote the therapeutic potential for cellular uptake by neural cells.

■ ASSOCIATED CONTENT

SI Supporting Information

The Supporting Information is available free of charge at <https://pubs.acs.org/doi/10.1021/acsbiomaterials.1c01487>.

Figure S1, spheroid size distribution for different conditions exposed to nanoscale iron oxides; Figure S2, additional flow cytometry results of the Live/Dead assay from two experiments for 8 nm treatments; Figure S3, MTT assay on cortical spheroids after 30 days of exposure to nanoscale iron oxides, Figure S4, flow cytometry of Ki67 expression for day 30 cortical spheroids. Figure S5, ICP-MS standard curve; Figure S6, dynamic light scattering of iron oxides; Table S1, list of antibodies; Table S2, primer sequence for target genes (PDF)

■ AUTHOR INFORMATION

Corresponding Authors

Yan Li – Department of Chemical and Biomedical Engineering, FAMU-FSU College of Engineering, Florida State University, Tallahassee, Florida 32310, United States; Institute of Molecular Biophysics, Florida State University, Tallahassee, Florida 32306, United States; orcid.org/0000-0002-5938-8519; Phone: 850-410-6320; Email: yli4@fsu.edu; Fax: 850-410-6150

Qing-Xiang Amy Sang – Department of Chemistry and Biochemistry, Florida State University, Tallahassee, Florida 32306, United States; Institute of Molecular Biophysics, Florida State University, Tallahassee, Florida 32306, United States; orcid.org/0000-0001-8828-0569; Phone: 850-644-8683; Email: qsang@fsu.edu; Fax: 850-644-8281

Authors

Elizabeth D. Henderson – Department of Chemistry and Biochemistry, Florida State University, Tallahassee, Florida 32306, United States; Present Address: Medicinal Chemistry at Presbyterian College School of Pharmacy, Clinton, South Carolina, United States

Timothy Hua – Department of Chemistry and Biochemistry, Florida State University, Tallahassee, Florida 32306, United States

Sonia Kiran – Department of Chemistry and Biochemistry, Florida State University, Tallahassee, Florida 32306, United States

Zahraa I. Khamis – Department of Chemistry and Biochemistry, Florida State University, Tallahassee, Florida 32306, United States; Department of Biochemistry, Faculty of Sciences-I, Lebanese University, Beirut 109991, Lebanon

Complete contact information is available at: <https://pubs.acs.org/doi/10.1021/acsbiomaterials.1c01487>

Author Contributions

[†]E.D.H., T.H., and S.K. contributed equally as co-first authors.

Notes

The authors declare no competing financial interest.

■ ACKNOWLEDGMENTS

The authors thank Dr. Brian K. Washburn and Kristina Poduch in the FSU Department of Biological Sciences for their help with RT-PCR analysis and the FSU Department of Biomedical Sciences for the support on flow cytometry analysis. Mark Marzano assisted E.H. in human stem cell stock culture. E.H. was supported by the Florida State University (FSU) Provost Postdoctoral Fellowship Program. This work was supported in part by grants from the Florida State University and an Endowed Chair Professorship in Cancer Research from anonymous donors to QXAS. This work is also partially supported by National Science Foundation (NSF CAREER award 1652992 to Y.L.).

■ REFERENCES

- (1) Thirupathi, A.; Chang, Y. Z. Brain Iron Metabolism and CNS Diseases. *Adv. Exp. Med. Biol.* **2019**, *1173*, 1–19.
- (2) Georgieff, M. K. Iron assessment to protect the developing brain. *Am. J. Clin. Nutr.* **2017**, *106* (Suppl 6), 1588S–1593S.
- (3) Cusick, S. E.; Georgieff, M. K.; Rao, R. Approaches for Reducing the Risk of Early-Life Iron Deficiency-Induced Brain Dysfunction in Children. *Nutrients* **2018**, *10* (2), 227.
- (4) Mezzaroba, L.; Alfieri, D. F.; Colado Simao, A. N.; Vissoci Reiche, E. M. The role of zinc, copper, manganese and iron in neurodegenerative diseases. *Neurotoxicology* **2019**, *74*, 230–241.
- (5) Soenen, S. J.; Himmelreich, U.; Nuytten, N.; De Cuyper, M. Cytotoxic effects of iron oxide nanoparticles and implications for safety in cell labelling. *Biomaterials* **2011**, *32* (1), 195–205.
- (6) Kim, H. Y.; Kim, T. J.; Kang, L.; Kim, Y. J.; Kang, M. K.; Kim, J.; Ryu, J. H.; Hyeon, T.; Yoon, B. W.; Ko, S. B.; Kim, B. S. Mesenchymal stem cell-derived magnetic extracellular nanovesicles for targeting and treatment of ischemic stroke. *Biomaterials* **2020**, *243*, 119942.
- (7) Maher, B. A. Airborne Magnetite- and Iron-Rich Pollution Nanoparticles: Potential Neurotoxicants and Environmental Risk Factors for Neurodegenerative Disease, Including Alzheimer's Disease. *J. Alzheimers Dis* **2019**, *71* (2), 361–375.
- (8) de Prado Bert, P.; Mercader, E. M. H.; Pujol, J.; Sunyer, J.; Mortamais, M. The Effects of Air Pollution on the Brain: a Review of Studies Interfacing Environmental Epidemiology and Neuroimaging. *Curr. Environ. Health Rep* **2018**, *5* (3), 351–364.
- (9) Chen, H.; Kwong, J. C.; Copes, R.; Tu, K.; Villeneuve, P. J.; van Donkelaar, A.; Hystad, P.; Martin, R. V.; Murray, B. J.; Jessiman, B.; Wilton, A. S.; Kopp, A.; Burnett, R. T. Living near major roads and the incidence of dementia, Parkinson's disease, and multiple sclerosis: a population-based cohort study. *Lancet* **2017**, *389* (10070), 718–726.
- (10) Crous-Bou, M.; Gascon, M.; Gispert, J. D.; Cirach, M.; Sanchez-Benavides, G.; Falcon, C.; Arenaza-Urquijo, E. M.; Gotsens, X.; Fauria, K.; Sunyer, J.; et al. Impact of urban environmental exposures on cognitive performance and brain structure of healthy individuals at risk for Alzheimer's dementia. *Environ. Int.* **2020**, *138*, 105546.
- (11) Calderon-Garciduenas, L.; Torres-Solorio, A. K.; Kulesza, R. J.; Torres-Jardon, R.; Gonzalez-Gonzalez, L. O.; Garcia-Arreola, B.; Chavez-Franco, D. A.; Luevano-Castro, S. C.; Hernandez-Castillo, A.; Carlos-Hernandez, E.; Solorio-Lopez, E.; Crespo-Cortes, C. N.; Garcia-

- Rojas, E.; Mukherjee, P. S.; Research Universidad del Valle de Mexico, U. V. M. G. Gait and balance disturbances are common in young urbanites and associated with cognitive impairment. Air pollution and the historical development of Alzheimer's disease in the young. *Environ. Res.* **2020**, *191*, 110087.
- (12) Petters, C.; Irrsack, E.; Koch, M.; Dringen, R. Uptake and metabolism of iron oxide nanoparticles in brain cells. *Neurochem. Res.* **2014**, *39* (9), 1648–60.
- (13) Maher, B. A.; Ahmed, I. A.; Karloukovski, V.; MacLaren, D. A.; Foulds, P. G.; Allsop, D.; Mann, D. M.; Torres-Jardon, R.; Calderon-Garciduenas, L. Magnetite pollution nanoparticles in the human brain. *Proc. Natl. Acad. Sci. U. S. A.* **2016**, *113* (39), 10797–801.
- (14) Tan, H. Y.; Cho, H.; Lee, L. P. Human mini-brain models. *Nat. Biomed Eng.* **2021**, *5* (1), 11–25.
- (15) Pasca, S. P. The rise of three-dimensional human brain cultures. *Nature* **2018**, *553* (7689), 437–445.
- (16) Lancaster, M. A.; Renner, M.; Martin, C. A.; Wenzel, D.; Bicknell, L. S.; Hurles, M. E.; Homfray, T.; Penninger, J. M.; Jackson, A. P.; Knoblich, J. A. Cerebral organoids model human brain development and microcephaly. *Nature* **2013**, *501* (7467), 373–9.
- (17) Del Dosso, A.; Urenda, J. P.; Nguyen, T.; Quadrato, G. Upgrading the Physiological Relevance of Human Brain Organoids. *Neuron* **2020**, *107* (6), 1014–1028.
- (18) Di Lullo, E.; Kriegstein, A. R. The use of brain organoids to investigate neural development and disease. *Nat. Rev. Neurosci.* **2017**, *18* (10), 573–584.
- (19) Marzano, M.; Bou-Dargham, M. J.; Cone, A. S.; York, S.; Helsper, S.; Grant, S. C.; Meckes, D. G., Jr.; Sang, Q. X.; Li, Y. Biogenesis of Extracellular Vesicles Produced from Human Stem Cell-Derived Cortical Spheroids Exposed to Iron Oxides. *ACS Biomaterials Science & Engineering* **2021**, *7* (3), 1111–1122.
- (20) Yan, Y.; Song, L.; Bejoy, J.; Zhao, J.; Kanekiyo, T.; Bu, G.; Zhou, Y.; Li, Y. Modelling neurodegenerative microenvironment using cortical organoids derived from human stem cells. *Tissue Engineering Part A* **2018**, *24* (13–14), 1125–1137.
- (21) Bejoy, J.; Song, L.; Wang, Z.; Sang, Q. X.; Zhou, Y.; Li, Y. Neuroprotective Activities of Heparin, Heparinase III, and Hyaluronic Acid on the A β 42-treated Forebrain Spheroids Derived from Human Stem Cells. *ACS Biomaterials Science & Engineering* **2018**, *4*, 2922–2933.
- (22) Song, L.; Yuan, X.; Jones, Z.; Vied, C.; Miao, Y.; Marzano, M.; Hua, T.; Sang, Q. X.; Guan, J.; Ma, T.; Zhou, Y.; Li, Y. Functionalization of Brain Region-specific Spheroids with Isogenic Microglia-like Cells. *Sci. Rep.* **2019**, *9*, 11055–11072.
- (23) Si-Tayeb, K.; Noto, F. K.; Sepac, A.; Sedlic, F.; Bosnjak, Z. J.; Lough, J. W.; Duncan, S. A. Generation of human induced pluripotent stem cells by simple transient transfection of plasmid DNA encoding reprogramming factors. *BMC Dev Biol.* **2010**, *10*, 81.
- (24) Si-Tayeb, K.; Noto, F. K.; Nagaoka, M.; Li, J.; Battle, M. A.; Duris, C.; North, P. E.; Dalton, S.; Duncan, S. A. Highly efficient generation of human hepatocyte-like cells from induced pluripotent stem cells. *Hepatology* **2010**, *51* (1), 297–305.
- (25) Yan, Y.; Martin, L.; Bosco, D.; Bundy, J.; Nowakowski, R.; Sang, Q. X.; Li, Y. Differential effects of acellular embryonic matrices on pluripotent stem cell expansion and neural differentiation. *Biomaterials* **2015**, *73*, 231–242.
- (26) Yan, Y.; Bejoy, J.; Xia, J.; Guan, J.; Zhou, Y.; Li, Y. Neural patterning of human induced pluripotent stem cells in 3-D cultures for studying biomolecule-directed differential cellular responses. *Acta Biomater.* **2016**, *42*, 114–126.
- (27) Yan, Y.; Li, Y.; Song, L.; Zeng, C.; Li, Y. Pluripotent stem cell expansion and neural differentiation in 3-D scaffolds of tunable Poisson's ratio. *Acta Biomater.* **2017**, *49*, 192–203.
- (28) Sart, S.; Bejarano, F. C.; Baird, M. A.; Yan, Y.; Rosenberg, J. T.; Ma, T.; Grant, S. C.; Li, Y. Intracellular labeling of mouse embryonic stem cell-derived neural progenitor aggregates with micron-sized particles of iron oxide. *Cytotherapy* **2015**, *17* (1), 98–111.
- (29) Yan, Y.; Calixto Bejarano, F.; Sart, S.; Muroski, M.; Strouse, G. F.; Grant, S. C.; Li, Y. Cryopreservation of embryonic stem cell-derived multicellular neural aggregates labeled with micron-sized particles of iron oxide for magnetic resonance imaging. *Biotechnol. Prog.* **2015**, *31* (2), 510–521.
- (30) Yan, Y.; Song, L.; Madinya, J.; Ma, T.; Li, Y. Derivation of cortical spheroids from human induced pluripotent stem cells in a suspension bioreactor. *Tissue Engineering Part A* **2018**, *24* (5–6), 418–431.
- (31) Sart, S.; Song, L.; Li, Y. Controlling redox status for stem cell survival, expansion and differentiation. *Oxidative Medicine and Cellular Longevity* **2015**, *2015*, 105135.
- (32) Alarifi, S.; Ali, D.; Alkahtani, S.; Alhader, M. S. Iron oxide nanoparticles induce oxidative stress, DNA damage, and caspase activation in the human breast cancer cell line. *Biol. Trace Elem. Res.* **2014**, *159* (1–3), 416–24.
- (33) Sajid, M.; Ilyas, M.; Basheer, C.; Tariq, M.; Daud, M.; Baig, N.; Shehzad, F. Impact of nanoparticles on human and environment: review of toxicity factors, exposures, control strategies, and future prospects. *Environmental Science and Pollution Research* **2015**, *22* (6), 4122–4143.
- (34) Sheikh, S.; Safia; Haque, E.; Mir, S. S. Neurodegenerative diseases: multifactorial conformational diseases and their therapeutic interventions. *J. Neurodegen. Dis.* **2013**, *2013*, 1.
- (35) Gh Popescu, B. F.; Nichol, H. Mapping brain metals to evaluate therapies for neurodegenerative disease. *CNS neuroscience & therapeutics* **2011**, *17* (4), 256–268.
- (36) Double, K.; Maywald, M.; Schmittel, M.; Riederer, P.; Gerlach, M. In vitro studies of ferritin iron release and neurotoxicity. *Journal of neurochemistry* **1998**, *70* (6), 2492–2499.
- (37) Cicero, C. E.; Mostile, G.; Vasta, R.; Rapisarda, V.; Signorelli, S. S.; Ferrante, M.; Zappia, M.; Nicoletti, A. Metals and neurodegenerative diseases. A systematic review. *Environmental research* **2017**, *159*, 82–94.
- (38) Zecca, L.; Youdim, M. B.; Riederer, P.; Connor, J. R.; Crichton, R. R. Iron, brain ageing and neurodegenerative disorders. *Nat. Rev. Neurosci.* **2004**, *5* (11), 863–873.
- (39) Cuajungco, M. P.; Lees, G. J. Zinc metabolism in the brain: relevance to human neurodegenerative disorders. *Neurobiology of disease* **1997**, *4* (3–4), 137–169.
- (40) Mocchegiani, E.; Bertoni-Freddari, C.; Marcellini, F.; Malavolta, M. Brain, aging and neurodegeneration: role of zinc ion availability. *Progress in neurobiology* **2005**, *75* (6), 367–390.
- (41) Madsen, E.; Gitlin, J. D. Copper and iron disorders of the brain. *Annu. Rev. Neurosci.* **2007**, *30*, 317–337.
- (42) Molina-Holgado, F.; Hider, R. C.; Gaeta, A.; Williams, R.; Francis, P. Metals ions and neurodegeneration. *Biomaterials* **2007**, *20* (3–4), 639–654.
- (43) Bush, A. I. Metals and neuroscience. *Curr. Opin. Chem. Biol.* **2000**, *4* (2), 184–191.
- (44) Zatta, P.; Frank, A. Copper deficiency and neurological disorders in man and animals. *Brain Research Reviews* **2007**, *54* (1), 19–33.
- (45) Sayre, L. M.; Zelasko, D. A.; Harris, P. L.; Perry, G.; Salomon, R. G.; Smith, M. A. 4-Hydroxynonenal-derived advanced lipid peroxidation end products are increased in Alzheimer's disease. *Journal of neurochemistry* **1997**, *68* (5), 2092–2097.
- (46) Smith, M. A.; Perry, G.; Richey, P. L.; Sayrec, L. M.; Anderson, V. E.; Beal, M. F.; Kowall, N. Oxidative damage in Alzheimer's. *Nature* **1996**, *382* (6587), 120–121.
- (47) Gabbita, S. P.; Lovell, M. A.; Markesbery, W. R. Increased nuclear DNA oxidation in the brain in Alzheimer's disease. *Journal of neurochemistry* **1998**, *71* (5), 2034–2040.
- (48) Calderón-Garciduenas, L.; Kavanaugh, M.; Block, M.; D'Angiulli, A.; Delgado-Chávez, R.; Torres-Jardón, R.; González-Maciél, A.; Reynoso-Robles, R.; Osnaya, N.; Villarreal-Calderon, R.; et al. Neuroinflammation, hyperphosphorylated tau, diffuse amyloid plaques, and down-regulation of the cellular prion protein in air pollution exposed children and young adults. *J. Alzheimer's Dis.* **2012**, *28* (1), 93–107.
- (49) Cacciottolo, M.; Wang, X.; Driscoll, I.; Woodward, N.; Saffari, A.; Reyes, J.; Serre, M. L.; Vizuete, W.; Sioutas, C.; Morgan, T. E. Particulate air pollutants, APOE alleles and their contributions to cognitive impair-

ment in older women and to amyloidogenesis in experimental models. *Transl. Psychiatry* **2017**, *7*, e1022.

(50) Gomma, I. O.; Kader, M. H.; Salah, T. A.; Heikal, O. A. Evaluation of in vitro mutagenicity and genotoxicity of magnetite nanoparticles. *Drug Discov Ther* **2013**, *7* (3), 116–23.

(51) Lee, J. R.; Park, B. W.; Kim, J.; Choo, Y. W.; Kim, H. Y.; Yoon, J. K.; Kim, H.; Hwang, J. W.; Kang, M.; Kwon, S. P.; Song, S. Y.; Ko, I. O.; Park, J. A.; Ban, K.; Hyeon, T.; Park, H. J.; Kim, B. S. Nanovesicles derived from iron oxide nanoparticles-incorporated mesenchymal stem cells for cardiac repair. *Sci. Adv.* **2020**, *6* (18), No. eaaz0952.

(52) Crichton, R. R.; Dexter, D.; Ward, R. J. Metal based neurodegenerative diseases—from molecular mechanisms to therapeutic strategies. *Coord. Chem. Rev.* **2008**, *252* (10–11), 1189–1199.

(53) Ighodaro, O. M.; Akinloye, O. A. First line defence antioxidants-superoxide dismutase (SOD), catalase (CAT) and glutathione peroxidase (GPX): Their fundamental role in the entire antioxidant defence grid. *Alexandria Journal of Medicine* **2018**, *54*, 287–293.

(54) Garcia-Caparros, P.; De Filippis, L.; Gul, A.; Hasanuzzaman, M.; Ozturk, M.; Altay, V.; Lao, M. T. Oxidative Stress and Antioxidant Metabolism under Adverse Environmental Conditions: a Review. *Bot. Rev.* **2021**, *87*, 421–466.

(55) Zhao, J.; Fu, Y.; Yamazaki, Y.; Ren, Y.; Davis, M. D.; Liu, C. C.; Lu, W.; Wang, X.; Chen, K.; Cherukuri, Y.; Jia, L.; Martens, Y. A.; Job, L.; Shue, F.; Nguyen, T. T.; Younkin, S. G.; Graff-Radford, N. R.; Wszolek, Z. K.; Brafman, D. A.; Asmann, Y. W.; Ertekin-Taner, N.; Kanekiyo, T.; Bu, G. APOE4 exacerbates synapse loss and neurodegeneration in Alzheimer's disease patient iPSC-derived cerebral organoids. *Nat. Commun.* **2020**, *11* (1), 5540.

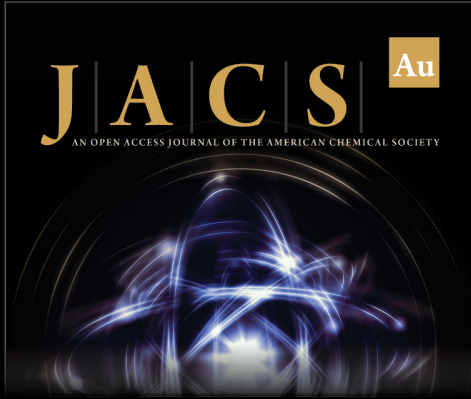
(56) Ooi, L.; Dottori, M.; Cook, A. L.; Engel, M.; Gautam, V.; Grubman, A.; Hernández, D.; King, A. E.; Maksour, S.; Targa Dias Anastacio, H.; et al. If human brain organoids are the answer to understanding dementia, what are the questions? *Neuroscientist* **2020**, *26* (5–6), 438–454.

(57) Hernandez, D.; Rooney, L. A.; Daniszewski, M.; Gulluyan, L.; Liang, H. H.; Cook, A. L.; Hewitt, A. W.; Pebay, A., Culture Variabilities of Human iPSC-Derived Cerebral Organoids Are a Major Issue for the Modelling of Phenotypes Observed in Alzheimer's Disease. *Stem Cell Rev. Rep* **2021**, DOI: 10.1007/s12015-021-10147-5.

(58) Quadrato, G.; Nguyen, T.; Macosko, E. Z.; Sherwood, J. L.; Min Yang, S.; Berger, D. R.; Maria, N.; Scholvin, J.; Goldman, M.; Kinney, J. P.; Boyden, E. S.; Lichtman, J. W.; Williams, Z. M.; McCarroll, S. A.; Arlotta, P. Cell diversity and network dynamics in photosensitive human brain organoids. *Nature* **2017**, *545* (7652), 48–53.

(59) Velasco, S.; Kedaigle, A. J.; Simmons, S. K.; Nash, A.; Rocha, M.; Quadrato, G.; Paulsen, B.; Nguyen, L.; Adiconis, X.; Regev, A.; Levin, J. Z.; Arlotta, P. Individual brain organoids reproducibly form cell diversity of the human cerebral cortex. *Nature* **2019**, *570* (7762), 523–527.

(60) Sart, S.; Tomasi, R. F.; Barizien, A.; Amselem, G.; Cumano, A.; Baroud, C. N. Mapping the structure and biological functions within mesenchymal bodies using microfluidics. *Sci. Adv.* **2020**, *6* (10), No. eaaw7853.



JACS Au
AN OPEN ACCESS JOURNAL OF THE AMERICAN CHEMICAL SOCIETY

Editor-in-Chief
Prof. Christopher W. Jones
Georgia Institute of Technology, USA

Open for Submissions 

pubs.acs.org/jacsau  ACS Publications
Most Trusted. Most Cited. Most Read.